Supplementary Information

Efficient growth of sub-micrometric MOF crystals inside the channels of AAO membranes

Mahmoud Maksoud, Nans Roques, Stéphane Brandès, Laurent Arurault, Jean-Pascal Sutter.

Experimental section.

Fig.

Fig. S1. FESEM images of the two faces of a CAAO membrane: a) side A; b) side B.

Fig. S2. FESEM images of the two faces of a CAAO membrane after solvothermal treatment in presence of $Cu(NO_3)_2$ and btc-H_3.

Fig. S3. FESEM images of the cross-section of a CAAO membrane after solvothermal treatment in presence of $Cu(NO_3)_2$ and btc-H_3.

Fig. S4. FESEM images of the cross-section of a CAAO membrane after 24 cycles of static SBS treatment.

Fig. S5. FESEM images of A (top) and B (bottom) faces for two different CAAO membranes after 12 and 24 cycles of static SBS treatment.

Fig. S6. FESEM images of the two faces of a CAAO membrane metallized with Pt: a) side A; b) side B.

Fig. S7. FESEM images of the cross-section of a metallized CAAO membrane after 12 cycles of dynamic SBS treatment.

Fig. S8. FESEM images of A (top) and B (bottom) faces for three different metallized CAAO membranes after 6 (a), 12 (b) and 24 (c) cycles of dynamic SBS treatment.

Fig. S9. IR spectra for reference samples and for composite membranes.

Fig. S10. XRPD patterns for reference samples and for composite membranes.

Figure S11. IR spectrum and XPRD pattern registered for a composite membrane stored 10 months in air.

Fig. S12. Influence of solvent and cycle duration on the amount of coordination polymer formed in the membrane central cross-section.

Fig. S13. FESEM images for (a) the A side of a metallized CAAO membrane after its treatment with a 10^{-3} M colloidal suspension of copper acetate, and (b) the central cross-section. (c) DLS histogram for the 10^{-3} M colloidal suspension of copper acetate.

Fig. S14. Variation for characteristic copper acetate, HKUST-1 and H_2O IR bands as a function of time during the membrane treatment with copper acetate colloids and btc-H_3 solutions, respectively.

Fig. S15. FESEM images of the cross-section of a metallized CAAO membrane after 2 cycles of dynamic SBS treatment with copper acetate colloids and btc-H_3 solutions.

Fig. S16. Color changes upon heating/cooling for CAAO composite membranes (H_2O release/uptake associated to the color change was evidenced by IR).

Fig. S17. (a) α_s-plot calculated for composite membranes. (b) Logarithm representation of the N_2 adsorption isotherms recorded at 77 K for pristine alumina membranes and composite membranes. (c) Pore size distribution calculated with the Horvath–Kawazoe method based on a cylindrical pore shape (Saito Foley) for reference HKUST-1 and for HKUST-1 loaded membrane

Fig. S18. (a) CO_2, N_2, O_2, CO and CH_4 adsorption /desorption isotherms for composite membranes at 298 K, 286 K and 273 K.

Fig. S19. Isosteric heat of composite membranes as a function of loading for CO, CO_2 and CH_4.

Tables

Table S1. Representative copper and carbon elemental analysis (%) for two metallized CAAO membranes after 24 cycles of dynamic SBS treatment.

Table S2. Calculated data of gas adsorption for HKUST@Al_2O_3.

Table S3. Selectivity for CO_2 adsorption at 298 K.

Experimental section.

Dynamic SBS setup:

Controlled flow-rate filtration was performed introducing the CAAO membranes in commercial Teflon filter-supports. Filtration flow-rates were controlled using programmable KDS-210 multichannel syringe pumps. To avoid the membrane occlusion by dust or undissolved reagents, the reagent solutions were systematically filtered through 200 nm Fluoropore membrane filters (Millipore). These filters were placed just before the Teflon supports holding the CAAO membranes. Membrane A side was systematically placed in such a way to face the reagent flow (see scheme below).
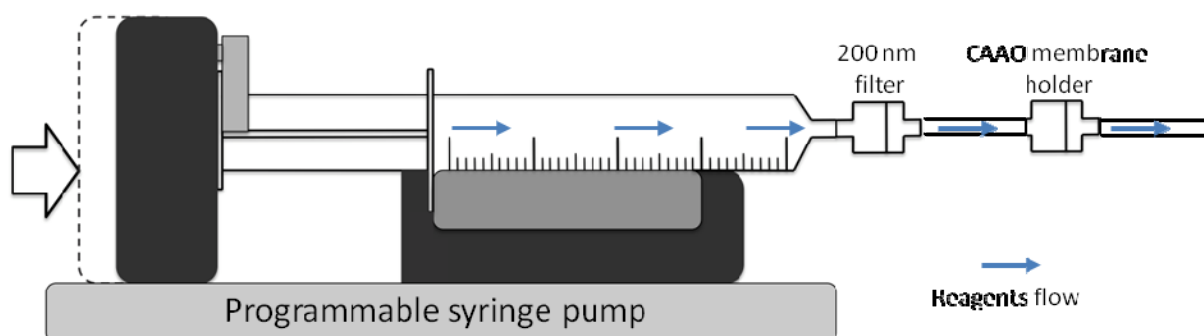
Gas sorption measurements

The isotherms were recorded at equilibrium for several relative pressure (P/P_0, P_0 = saturated vapor pressure) in a large range of P/P_0 (10^{-7} to 1). The specific surface area were determined by physisorption of N_2 at 77 K using the standard BET method[1] assuming a monolayer coverage of N_2 and a cross-sectional area of 16.2 $Å^2$/molecule.

The BET assumption is *a priori* non-valid for microporous solids over the usual range $0.05 < P/P_0 < 0.25$ but it can be used if care is taken to choose a suitable pressure range for which the BET analysis can be applied. As required by Snurr[2] and Rouquerol,[3] the pressure range selected should give increasing values of $V \times (P_0-P)$ with P/P_0. Hence, five points with pressures $P/P_0 < 0.04$ were used for BET analyses of HKUST-1 functionalized membranes.

The total surface area S_t is assumed to be equal to S_{BET}. The total pore volume was estimated directly from the isotherm at $P/P_0 = 0.99$. The mesopore volume V_M, the micropore volume V_m, and the external surface area S_{ext} were obtained using the α_s-plot method.[4-6] The macroporous Polygoprep® 1000-50 silica gel (Macherey-Nagel) with $S_{BET} = 29.8$ $m^2 \cdot g^{-1}$ was

used as a reference adsorbent. The presence of linear segments on the α_s curves indicates that, in the pressure range of the study, the course of adsorption on a given sample is the same as the course of adsorption for the reference adsorbent. Both the slope of these linear segments and the intercept can thus be used to estimate the volume and the surface area of the external and microporous part of the sample. Since the mesoporous part is minor and represents a quite broad distribution of pores, V_M and S_M were estimated from the BJH calculations.[7] The micropore diameter for HKUST-1 functionalized membranes was also estimated from adsorption isotherms using the Horvath-Kawazoe method with a cylindrical-shape pore geometry (Saito-Foley).

Composite materials reactivity towards CO_2, CH_4, CO and N_2 was analysed by recording the adsorption isotherms at 298, 287 and 273 K using the same analytical apparatus. This allowed calculating the isosteric heat of adsorption by applying the Clausius-Clapeyron equation:

$$\frac{\partial lnP}{\partial(1/T)} = -\frac{\Delta H}{R}$$

where ΔH is the heat of adsorption, P the pressure, R the gas constant and T the temperature.
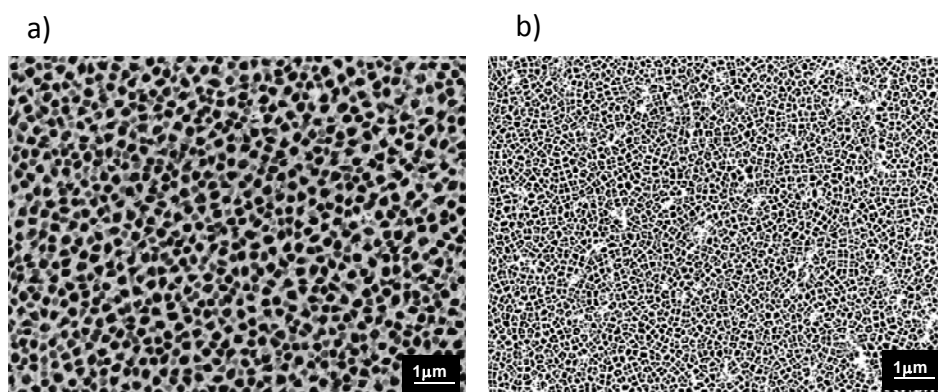
Preparation of bulk HKUST-1:

Bulk HKUST-1 was prepared following a known procedure.[8] A solution of $Cu(NO_3)_2 \cdot 2.5H_2O$ (12.3 mmol, 2.86 g) in 40.5 mL of deionized H_2O was mixed with a solution of btc-H_3 (8.2 mmol, 1.701 g) in the same volume of absolute EtOH. After 10 minutes under agitation at room temperature, the mixture was transferred into a 100 mL Teflon-lined autoclave and progressively warmed-up to reach 120°C. After 24 h, the temperature was slowly cooled down to RT. The crude HKUST-1 material was recovered by filtration and purified through 30 min reflux in acetone: EtOH solvent mixture. After drying, pure HKUST-1 is recovered as a blue microcrystalline powder in 55% yield with respect to $Cu(NO_3)_2 \cdot 2.5H_2O$. This compound was used as a reference for IR, XRD and sorption measurements.

IR (v, cm^{-1}, KBr): v = 734,760, 1043, 1111, 1375, 1448, 1590, 1645, 3430.
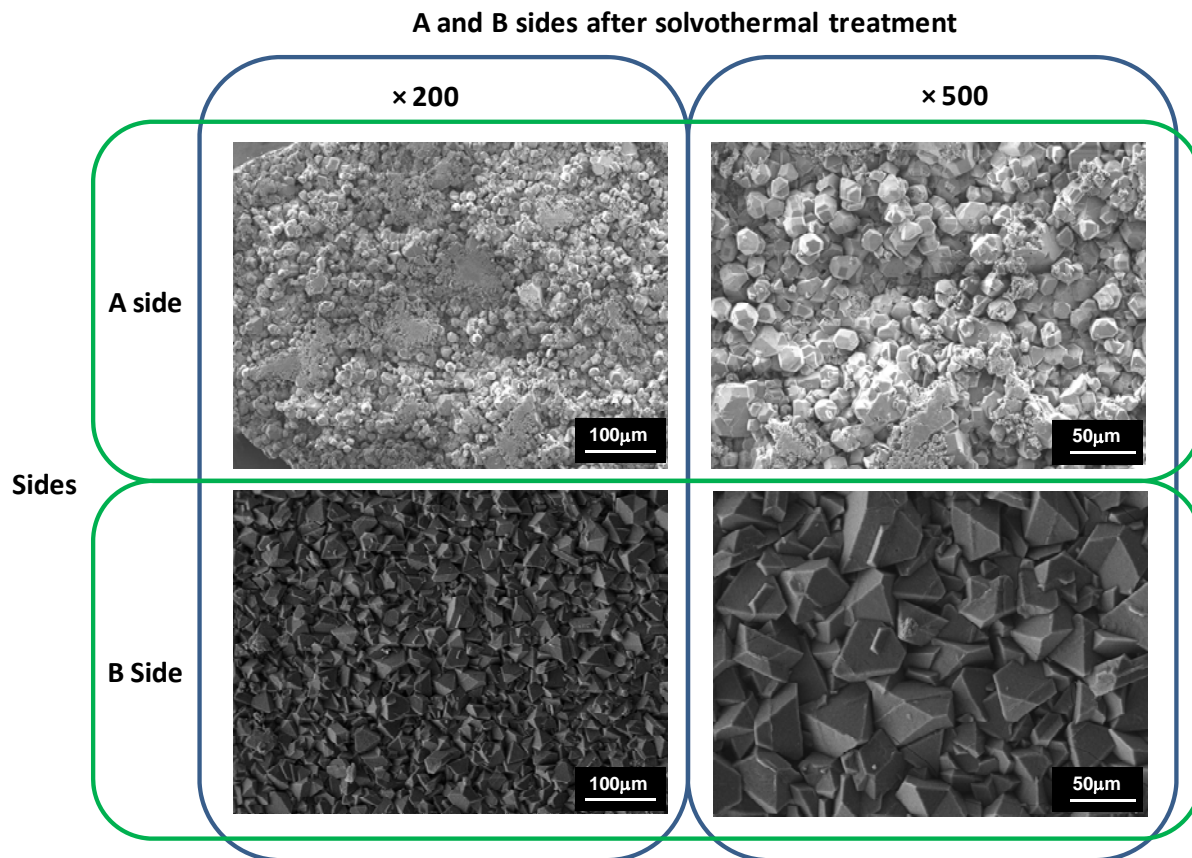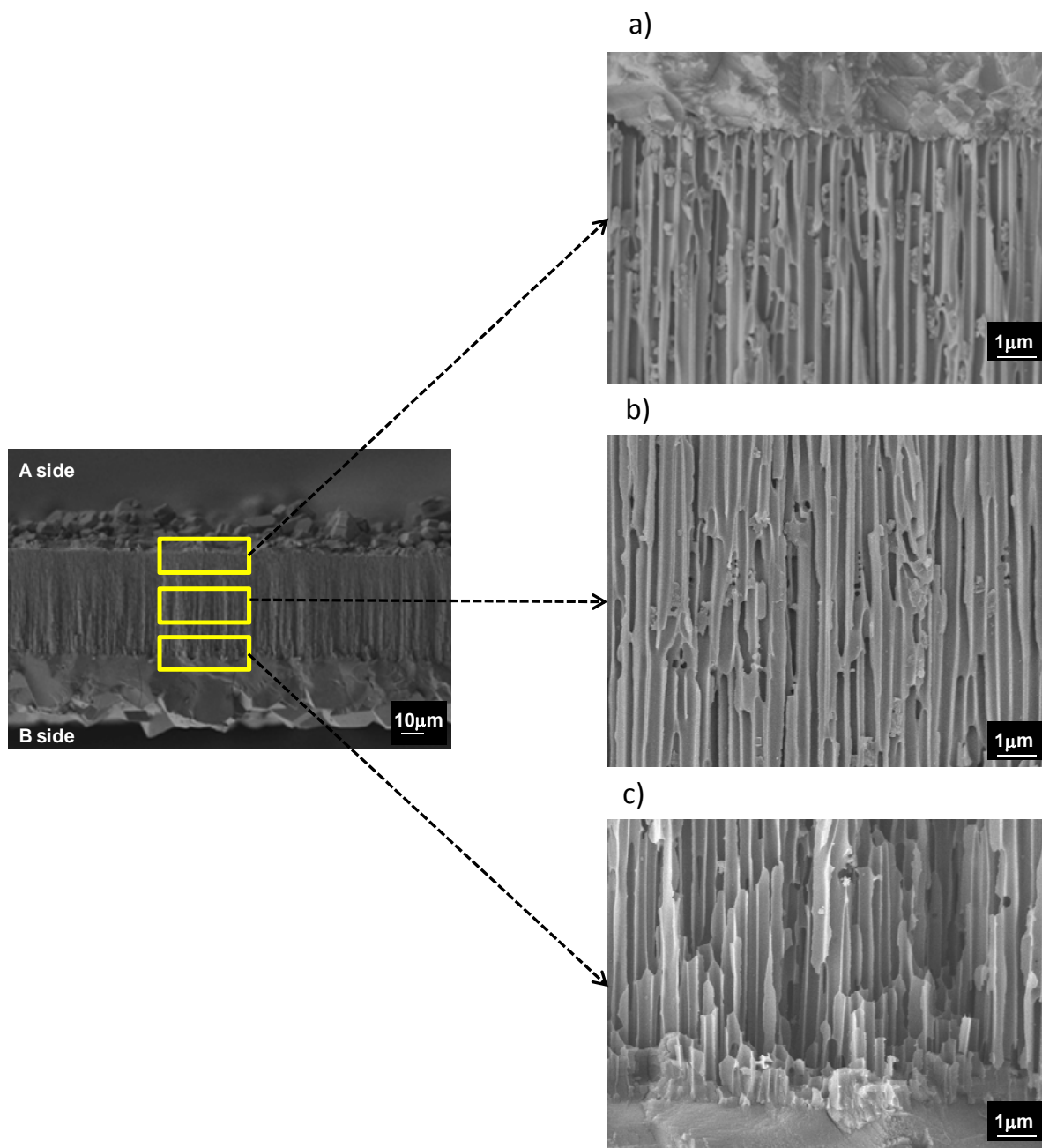
Figures

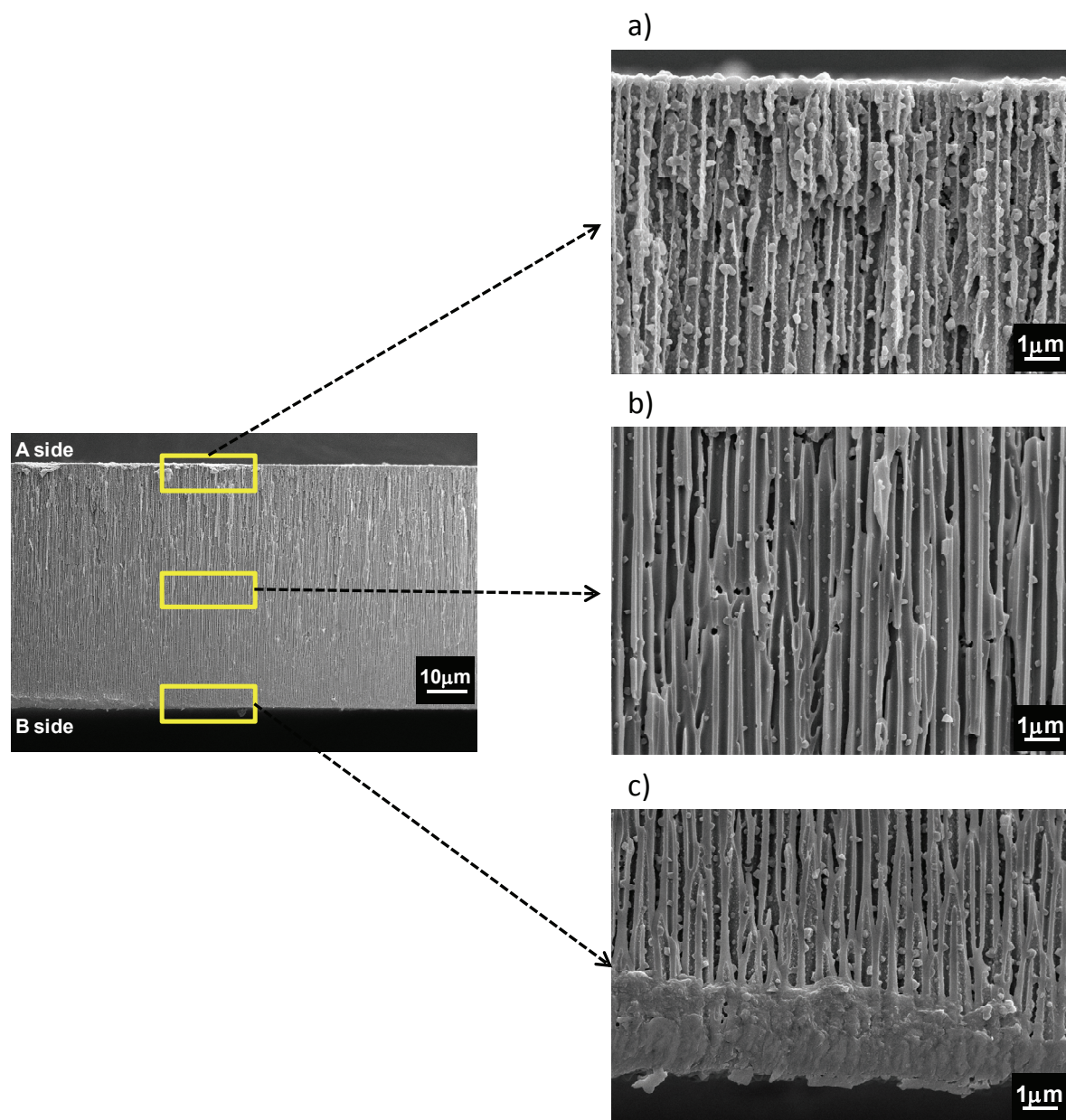**Fig. S1** FESEM images of the two faces of a CAAO membrane: a) side A; b) side B.

a)   b)

Fig. S2 FESEM images of the two faces of a CAAO membrane after solvothermal treatment in presence of $Cu(NO_3)_2$ and btc-H_3.

A and B sides after solvothermal treatment

Fig. S3 FESEM images of the cross-section of a CAAO membrane after solvothermal treatment in presence of $Cu(NO_3)_2$ and btc-H_3.
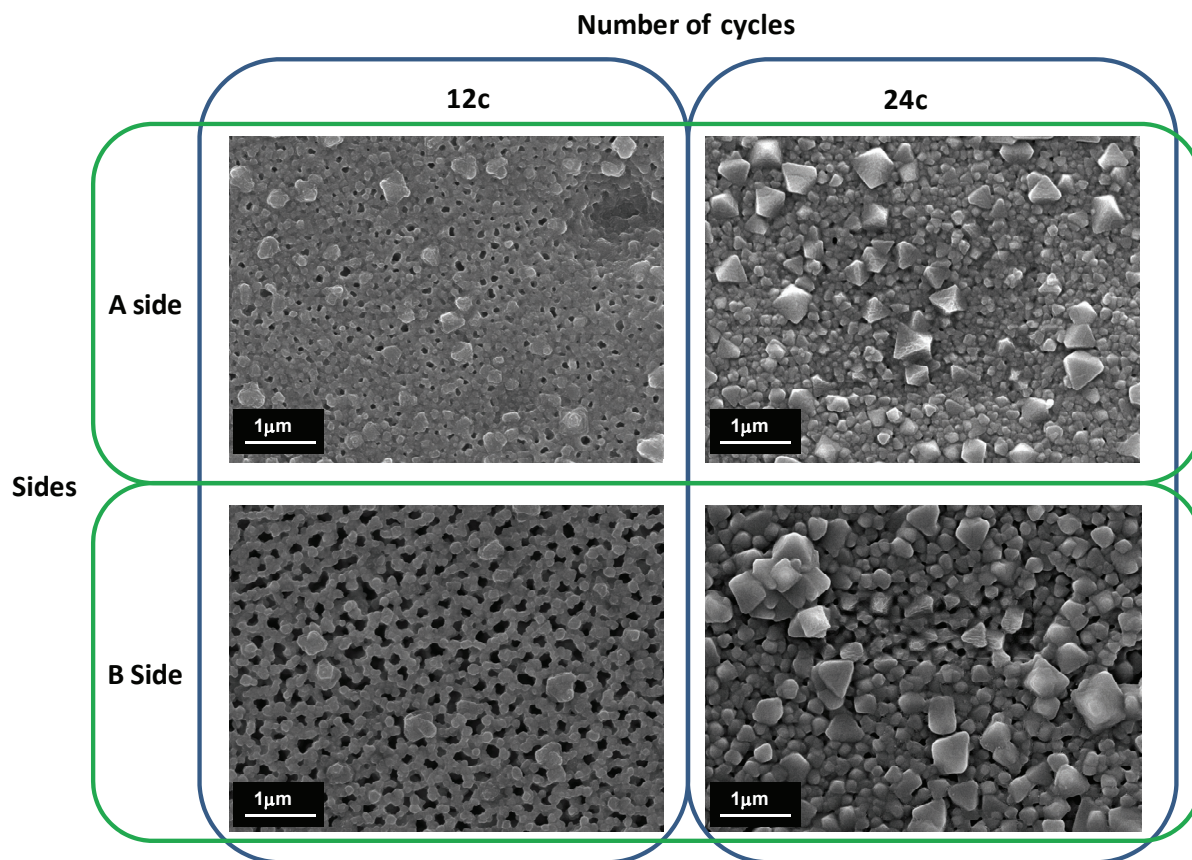
Fig. S4 FESEM images of the cross-section of a CAAO membrane after 12 cycles of static SBS treatment.

a)

b)

c)

Fig. S5 FESEM images of A (top) and B (bottom) faces for two different CAAO membranes after 12 and 24 cycles of static SBS treatment.
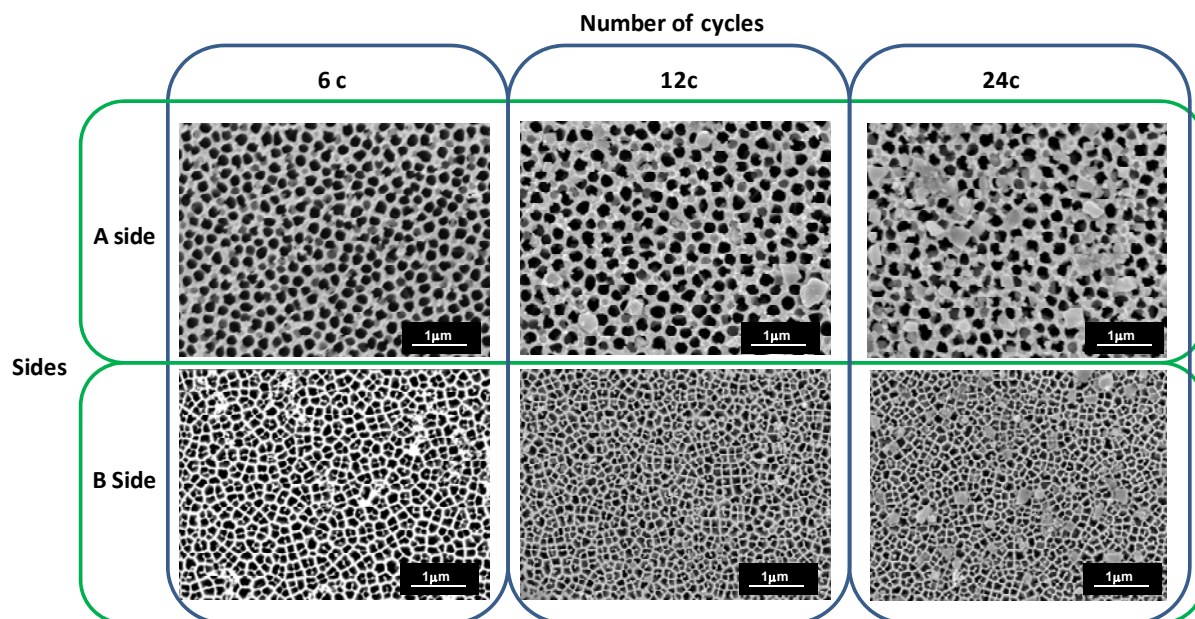

Fig. S6 FESEM images of the two faces of a CAAO membrane metallized with Pt: a) side A; b) side B.

Fig. S7 FESEM images of the cross-section of a metallized CAAO membrane after 12 cycles of dynamic SBS treatment.

Fig. S8 FESEM images of A (top) and B (bottom) faces of three different metallized CAAO membranes after 6 (a), 12 (b) and 24 (c) cycles of dynamic SBS treatment.


Fig. S9 IR spectra for reference samples and for composite membranes. (a) CAAO Whatman Anodisc, (b, KBr pellets) bulk HKUST-1, (c, KBr pellets) CAAO membrane after solvothermal treatment, (d) CAAO membrane after 24 cycles of static SBS treatment, (e) metallized CAAO membrane after 24 cycles of dynamic SBS treatment, (f) metallized CAAO membrane after 2 cycles of dynamic SBS treatment using colloidal suspension of copper acetate.
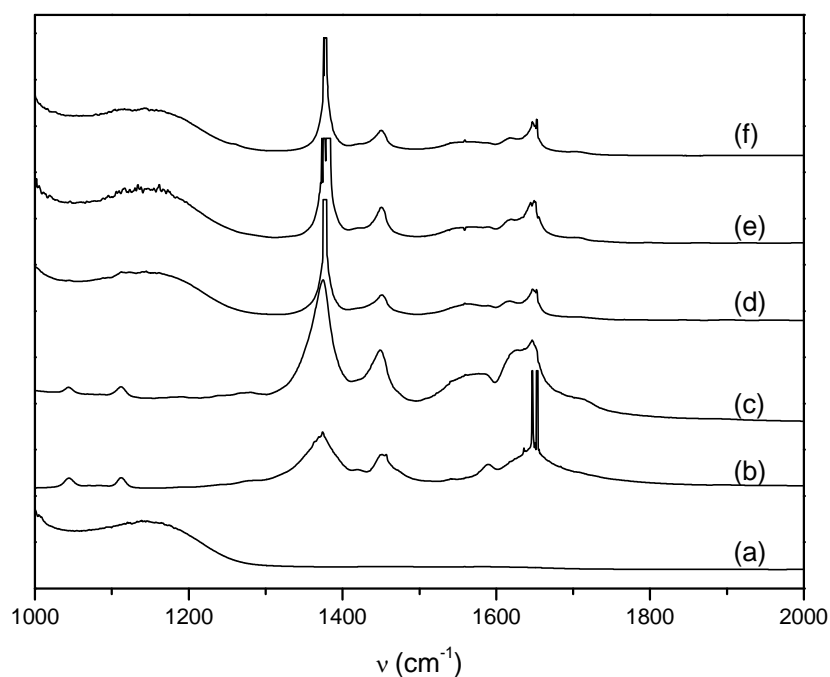
Fig. S10 (a) Simulated XRPD pattern for HKUST-1 and experimental XRPD patterns for: (b) bulk material, (c) a CAAO membrane after solvothermal treatment, (d) a CAAO membrane after 24 cycles of classical SBS treatment, (e) a metallized CAAO membrane after 12 cycles of dynamic SBS treatment and (f) a metallized CAAO membrane after 2 cycles of dynamic SBS treatment using colloidal suspension of copper acetate. Presence/lack of XRD peak observed for 2θ values close to $6°$ depends on the amount of H_2O molecules located in the MOF architecture.[9]
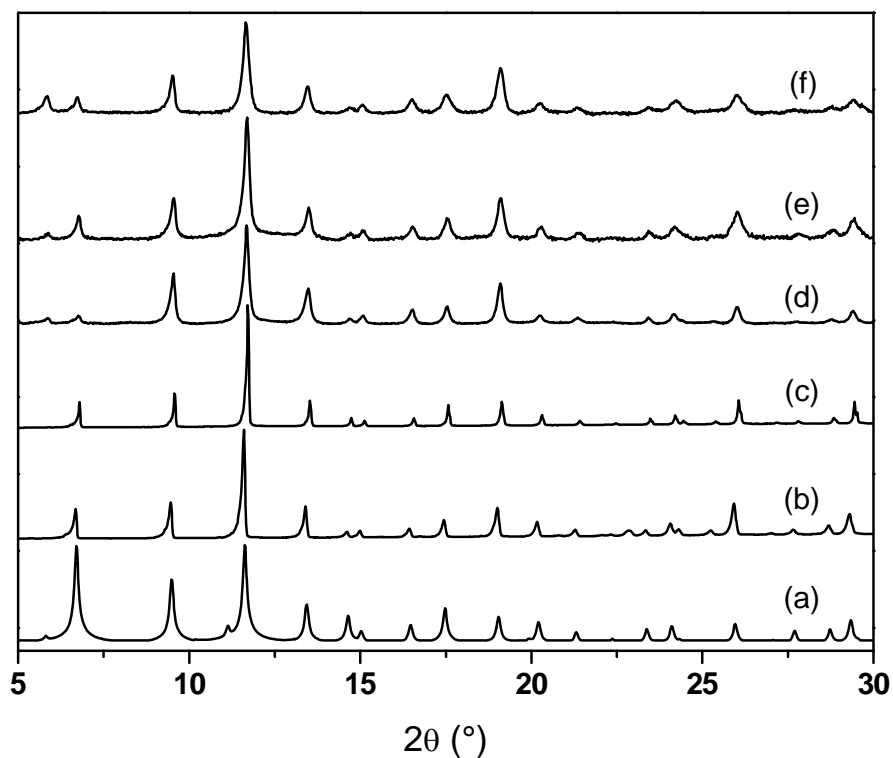
Figure S11. Composite membrane aging: (*Top)* IR spectra for a composite membrane (a) as-synthesized and (b) same membrane stored 10 months in air; *(Bottom)* XPRD pattern for the aged membrane (b) compared to the pattern simulated from HKUST-1 crystallographic data (a).
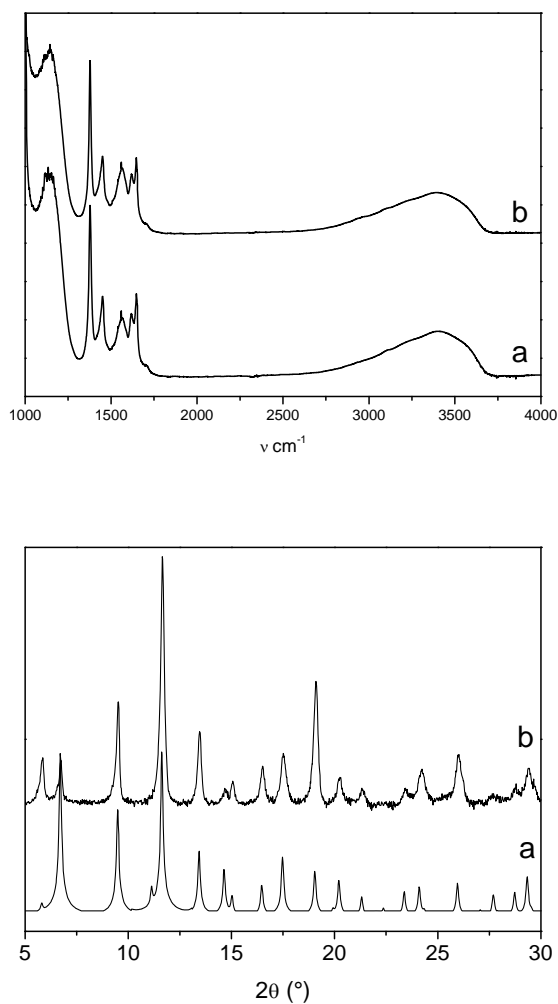
Fig. S12 Influence of solvent and cycle duration on the amount of coordination polymer formed in the membrane central cross-section.
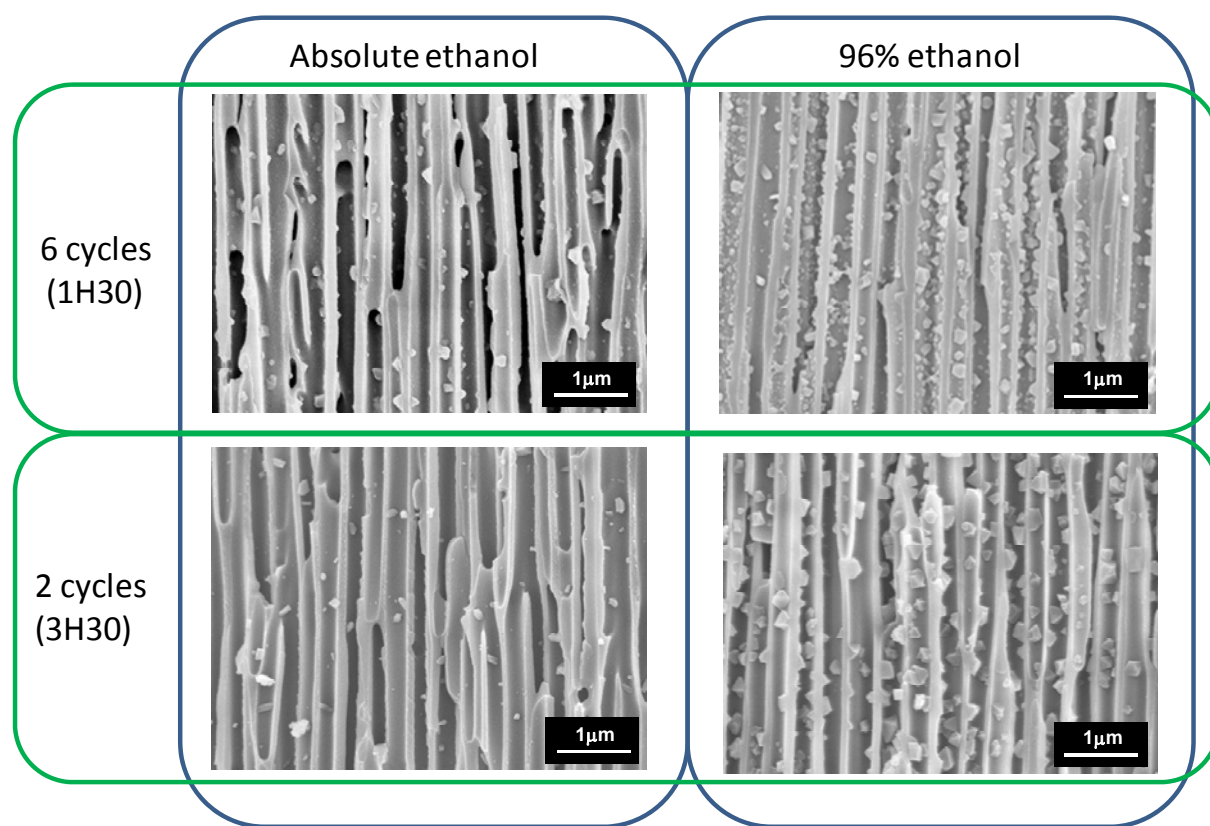

Fig. S13 FESEM images for (a) the A side of a metallized CAAO membrane after its treatment with a 10^{-3} M colloidal suspension of copper acetate (before the cleaning step with ethanol), and (b) the central cross-section (after the cleaning step with ethanol). (c) DLS histogram for the 10^{-3} M colloidal suspension of copper acetate.
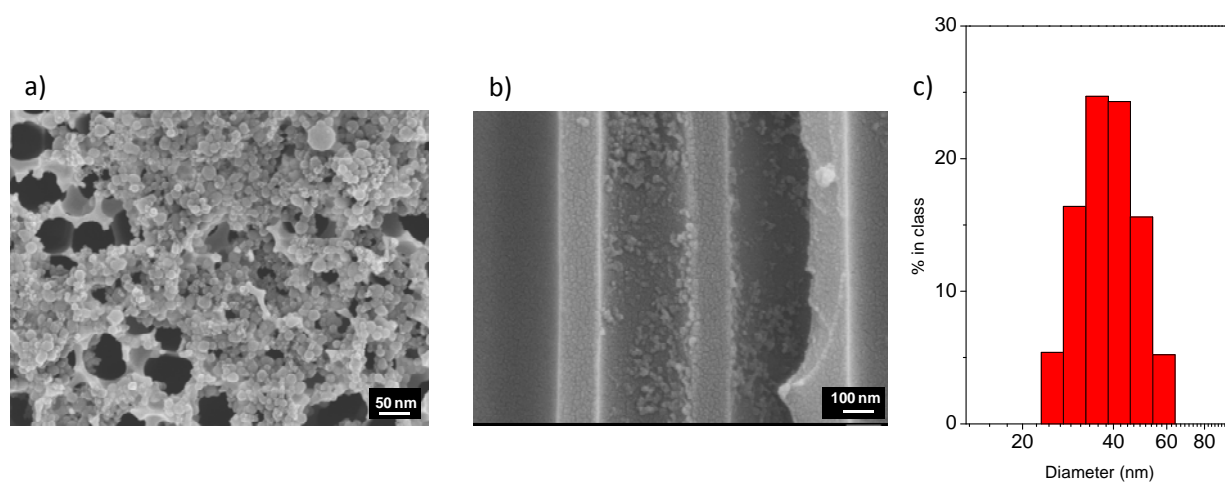
Fig. S14 Variation for characteristic copper acetate ((a), 1500-1600 cm^{-1}), HKUST-1 ((b), 1330-1400 cm^{-1} and, (c), 1425-1480 cm^{-1}) and H$_2$O ((d), 2800-3750 cm^{-1}) IR bands as a function of time during the membrane treatment with copper acetate colloids and btc-H$_3$ solutions, respectively. Membrane was cleaned with 96% ethanol before each IR measurement.
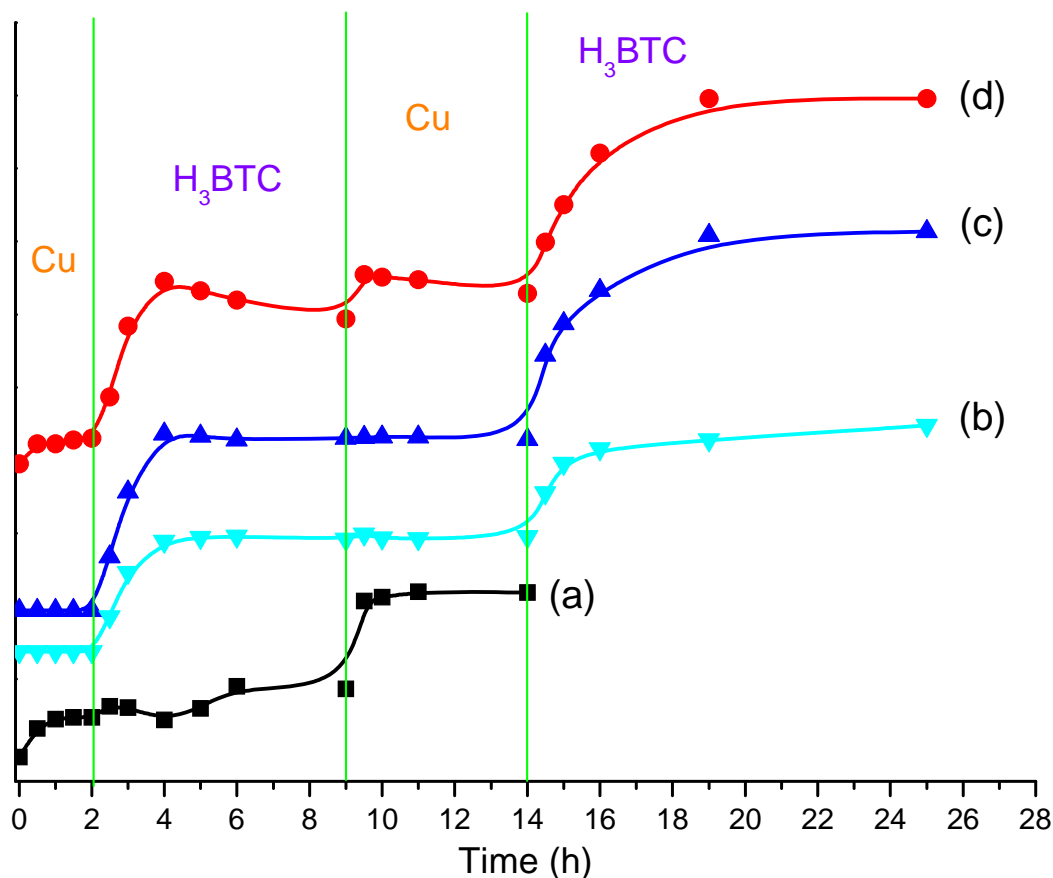
Fig. S15 FESEM images of the cross-section of a metallized CAAO membrane after 2 cycles of dynamic SBS treatment with copper acetate colloids and btc-H_3 solutions.
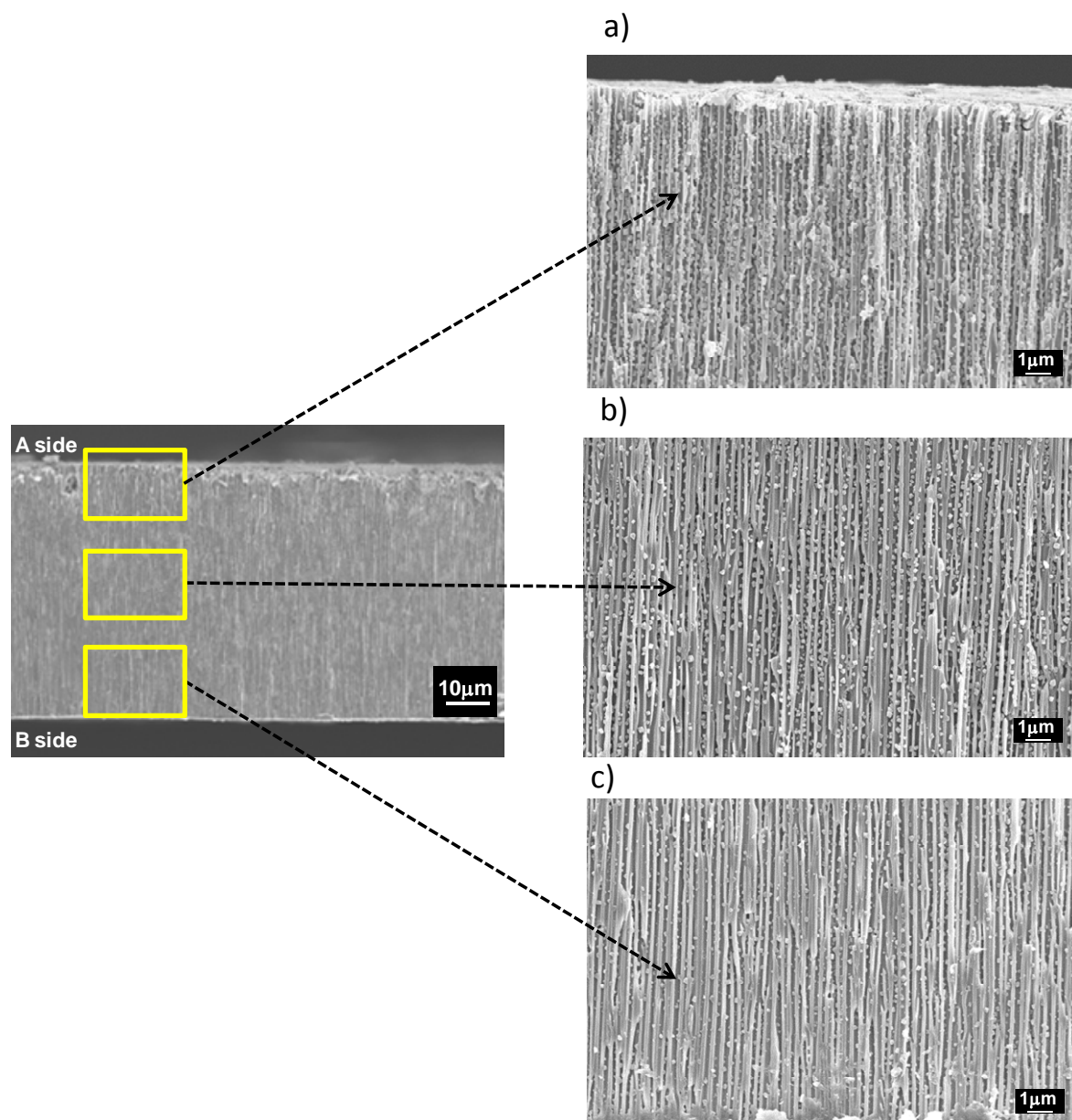
Fig. S16 Color changes upon heating/cooling for CAAO composite membranes (H_2O release/uptake associated to the color change was evidenced by IR).
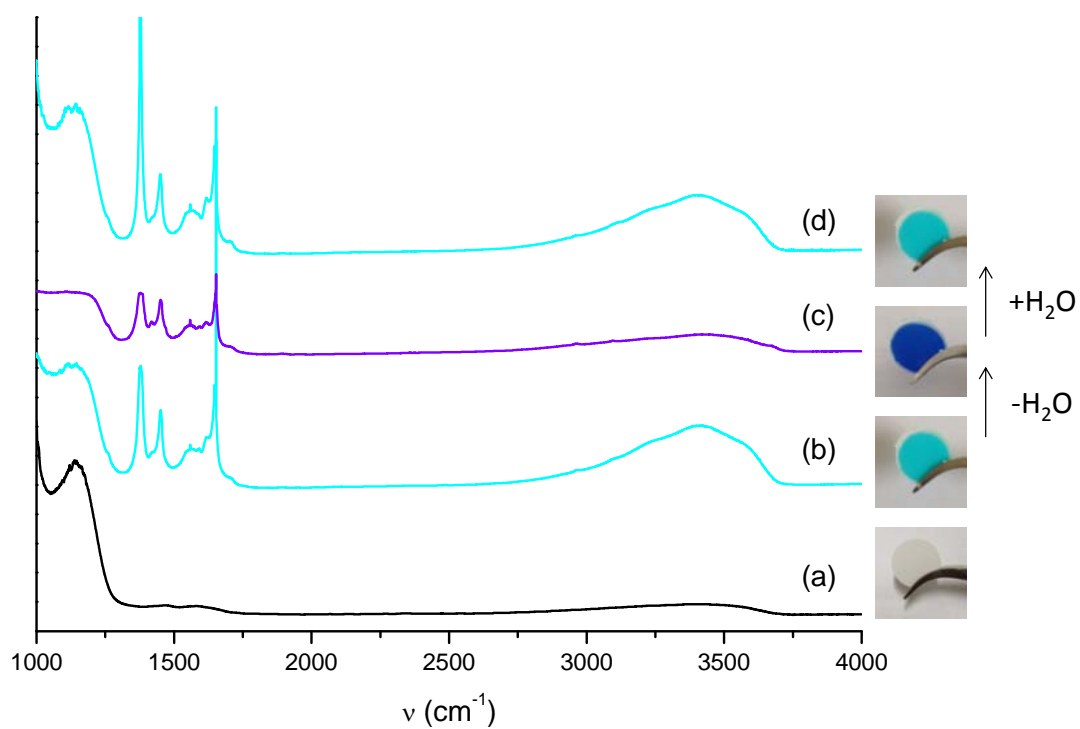
Fig. S17 (a) α_s-plot calculated for composite membranes. (b) Logarithm representation of the N_2 adsorption isotherms recorded at 77 K for pristine alumina membranes (bottom) and composite membranes (top). (c) Pore size distribution calculated with the Horvath–Kawazoe method based on a cylindrical pore shape (Saito Foley) for reference HKUST-1 (blue) and for HKUST-1 loaded membrane (red).

a)

b)

c)

17
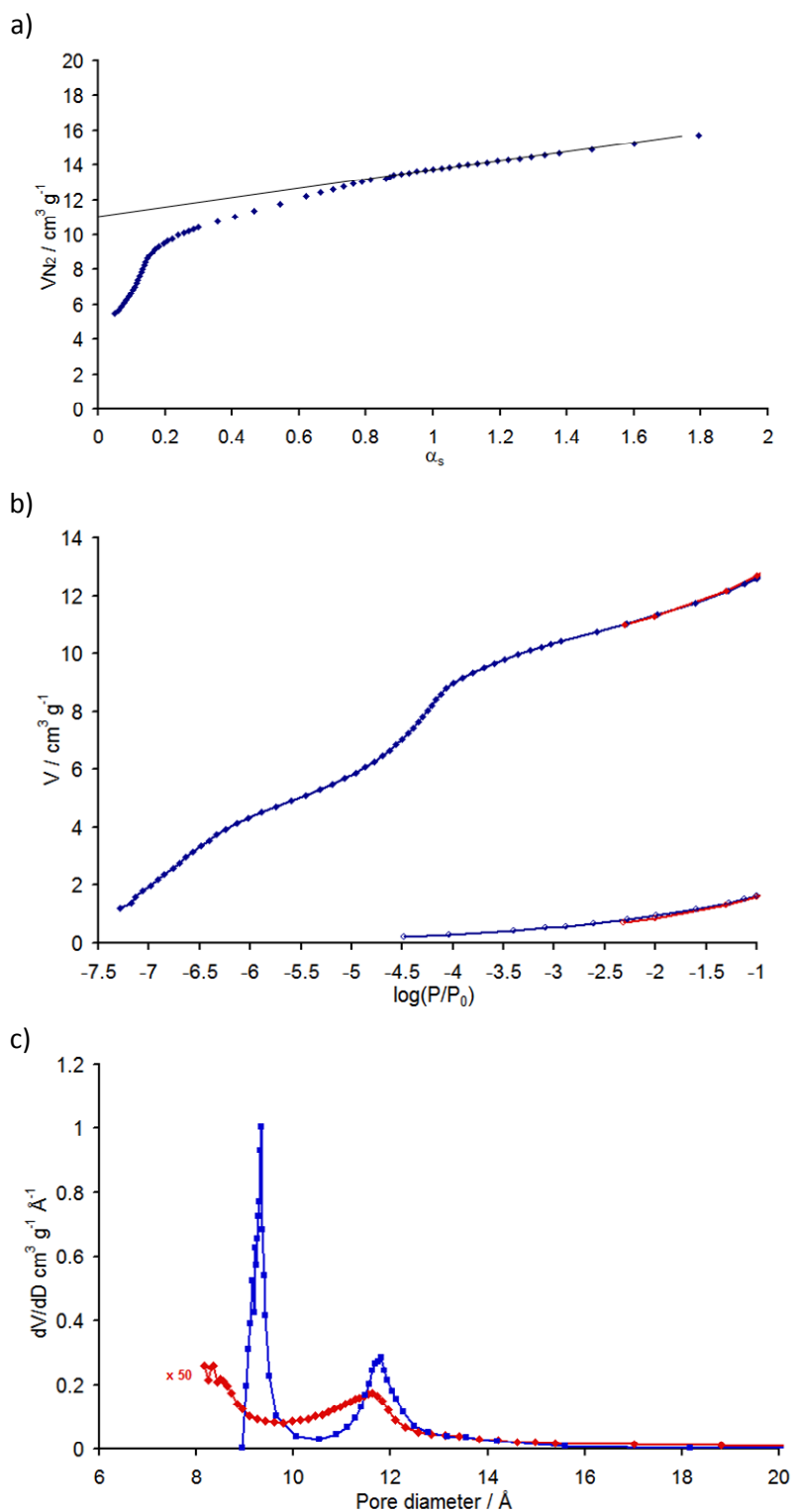
Fig. S18 (a) CO_2, N_2, O_2, CO and CH_4 adsorption (solid lines)/desorption (dashed lines) isotherms for composite membranes. (b) CO (dashed lines) and CH_4 (solid line) adsorption/desorption isotherms of composite membranes recorded at 298 K (blue lines), 286 K (black line) and 273 K (red line).

a)

b)
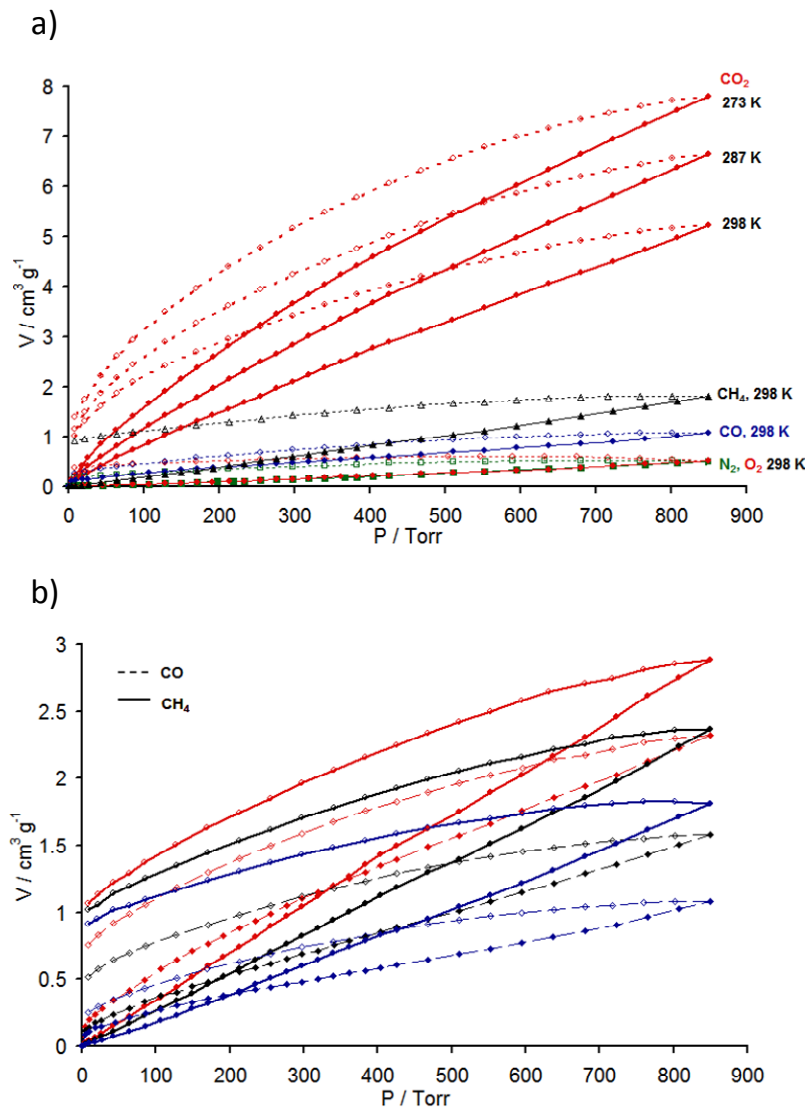
Fig. S19 Isosteric heat of composite membranes for CO (black lines), CO_2 (blue line) and CH_4 (red line) as a function of loading.
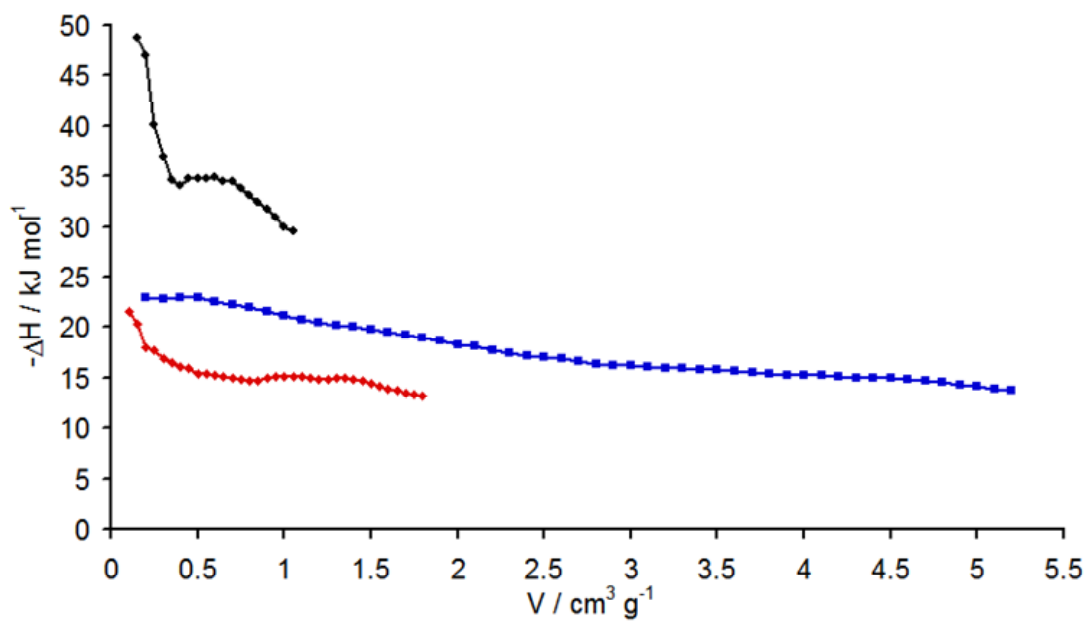
Tables

Table S1 Representative copper and carbon elemental analysis (%) for two metallized CAAO membranes after 24 cycles of dynamic SBS treatment.

Sample	C(%)[a]	Corrected C (%) [a,b]	Cu (%)	HKUST-1 from C %	HKUST-1 from Cu %
			Composition		
			Pristine CAAO membranes		
	0.26	0	0	0	0
			Composite membranes		
Membrane 1	1.39	1.13	1.06	3.66	3.44
Membrane 2	1.87	1.61	1.70	5.80	4.90

[a] Average values. [b] Corrected values obtained removing the carbon percentage for pristine membranes from the average carbon percentage obtained for composite membranes.

Table S2 Calculated data of gas adsorption for HKUST@Al_2O_3.

	V_1[a] [$cm^3 \cdot g^{-1}$]	$(K_{CO_2})_1$[b] [$Torr^{-1}$]	V_2[a] [$cm^3 \cdot g^{-1}$]	$(K_{CO_2})_2$[b] [$Torr^{-1}$]	Henry constant[c] [$cm^3 \cdot g^{-1} \cdot Torr^{-1}$]
CO_2	40.4	1.64×10^{-4}	0.24	3.8×10^{-2}	1.57×10^{-2}
CO	20.0	5.41×10^{-5}	0.17	0.18	3.07×10^{-2}
CH_4	170.3	1.23×10^{-5}	–	–	2.09×10^{-3}
N_2	77.4	7.18×10^{-6}	–	–	5.56×10^{-4}
O_2	84.2	6.63×10^{-6}	–	–	5.59×10^{-4}

[a] Calculated saturation volume of the mono– or dual–site Langmuir model. [b] Calculated stability constants of the mono– or dual–site Langmuir model. [c] Henry constant = $K_1 \times V_1 + K_2 \times V_2$ or $K_i \times V_i$ ($cm^3 \cdot g^{-1} \cdot Torr^{-1}$).

Table S3 Selectivity for CO_2 adsorption at 298 K.

	$S_{CO_2/CO}$	S_{CO_2/CH_4}	S_{CO_2/O_2}	S_{CO_2/N_2}
Selectivity at zero loading[a]	0.5	7.5	28.1	28.2
Selectivity for an equimolar gas mixture[b]	4.7	3.4	13.0	14.2

[a] Calculated by the Henry ratio constant. [b] Calculated for a total pressure equal to 1 atm.

Sorption selectivities and heats of adsorption determination

Sorption selectivities were calculated using a dual site Langmuir equation for CO_2 and CO isotherms.[10-12] Perfect adjustments were obtained using this model equation, in agreement with different energy interactions with the material surface for these gases. Nevertheless, the fact that one contribution largely dominates when saturation capacities are considered means that the material presents nearly homogeneous adsorption sites (see Table S2). For other gases, no specific interaction occurs since a single Langmuir isotherm of Henry–type is enough to fit the isotherms. Corresponding Henry constants were used to evaluate the selectivity for CO_2 at zero coverage. Values found for this gas over CO, CH_4, O_2 and N_2 are given in Table S3. The unexpected selectivity observed for CO at low loadings when compared with the bulk material is ascribed to the platinum film deposited on the membranes external faces to enable selective MOF growth into their channels.[13-15] Selectivities evidenced for CO_2 over N_2, O_2 and CH_4 are in good agreement with the ones reported for the bulk HKUST-1. Electrostatic interactions of CO_2 with this latter material are dominated by the high quadrupolar moment presented by this gas molecule because copper metal sites behave as weak Lewis acids and are often hindered or not accessible in the activated material.[14, 16] The weak quadrupolar moment of N_2 and O_2 explains their very low affinity for this MOF as a bulk, and, therefore, the high selectivity for CO_2 *vs* N_2 and O_2 shown by HKUST-1 loaded membranes (Table S3). A higher adsorption capacity is also observed for CH_4 over CO despite the absence of any dipolar or quadrupolar moment for CH_4. When the material pores are progressively filled, dispersion interactions occur and the large polarizability of CH_4 results in a significantly higher adsorption as compared with CO. CH_4 adsorption is however much lower than the one observed for CO_2.

CO_2, CO and CH_4 heats of adsorption were determined with the Clausius-Clapeyron analysis by recording isotherms at 273, 287 and 298 K. As expected, both the adsorption capacity and the electrostatic interactions increase as the temperature is lowered. At 298 K (Fig. S19), the enthalpy at zero coverage is -23 kJ mol^{-1} for CO_2. This value is in good agreement with literature data.[14, 15, 17] Together with the slight decrease observed as a function of loading, it indicates moderate interaction of CO_2 with the open metal sites like for pure HKUST. The higher isosteric heat at low coverage exhibited for CO is probably due to its dipole, which favours stronger interactions of this gas with the metal centers than for CO_2, but a significant contribution probably comes from platinum films, as suggested above. For CH_4, decrease of the enthalpy as a function of loading is also observed. The energy is lower than for CO and CO_2, in agreement with the lower affinity and capacity for CH_4 *vs* CO_2.

REFERENCES

1. S. Brunauer, P. H. Emmet and E. Teller, *J. Am. Chem. Soc.*, 1938, **60**, 309-319.
2. K. S. Walton and R. Q. Snurr, *J. Am. Chem. Soc.*, 2007, **129**, 8552-8556.
3. J. Rouquerol, P. Llewellyn and F. Rouquerol, *Studies in Surface Science and Catalysis*, 2007, **160**, 49-56.
4. M. Kruk, M. Jaroniec, R. Ryoo and J. M. Kim, *Microporous Materials*, 1997, **12**, 93-106.
5. A. Sayari, P. Liu, M. Kruk and M. Jaroniec, *Chem. Mater.*, 1997, **9**, 2499-2506.
6. K. S. W. Sing, D. H. Everett, R. A. W. Haul, L. Moscou, R. A. Pierotti, J. Rouquérol and T. Siemieniewska, *Pure Appl. Chem.*, 1985, **57**, 603-619.
7. E. Barrett, L. G. Joyner and P. P. Halenda, *J. Am. Chem. Soc.*, 1951, **73**, 373-380.
8. M. Schlesinger, S. Schulze, M. Hietschold and M. Mehring, *Micropor. Mesopor. Mater.*, 2010, **132**, 121-127.
9. K. Schlichte, T. Kratzke and S. Kaskel, *Micoporous Mesoporous Mater.*, 2004, **73**, 81-88.
10. S. Brandès, G. David, C. Suspène, R. J. P. Corriu and R. Guilard, *Chem. Eur. J.*, 2007, **13**, 3480-3490.
11. G. Ortiz, S. Brandes, Y. Rousselin and R. Guilard, *Chem. - Eur. J.*, 2011, **17**, 6689-6695.
12. C. Suspene, S. Brandes and R. Guilard, *Chem. - Eur. J.*, 2010, **16**, 6352-6364.
13. P. Chowdhury, C. Bikkina, D. Meister, F. Dreisbach and S. Gumma, *Microporous Mesoporous Mater.*, 2009, **117**, 406-413.
14. P. Chowdhury, S. Mekala, F. Dreisbach and S. Gumma, *Microporous Mesoporous Mater.*, 2012, **152**, 246-252.
15. Q. M. Wang, D. M. Shen, M. Bulow, M. L. Lau, S. G. Deng, F. R. Fitch, N. O. Lemcoff and J. Semanscin, *Microporous Mesoporous Mater.*, 2002, **55**, 217-230.
16. A. O. Yazaydin, R. Q. Snurr, T.-H. Park, K. Koh, J. Liu, M. D. LeVan, A. I. Benin, P. Jakubczak, M. Lanuza, D. B. Galloway, J. J. Low and R. R. Willis, *J. Am. Chem. Soc.*, 2009, **131**, 18198-+.
17. L. Grajciar, A. D. Wiersum, P. L. Llewellyn, J.-S. Chang and P. Nachtigall, *J. Phys. Chem. C*, 2011, **115**, 17925-17933.